

## **Novel back contact reflector for high efficiency and double graded Cu(In,Ga)Se<sub>2</sub> thin film solar cells**

Benjamin Bissig, Romain Carron, Lukas Greuter, Shiro Nishiwaki, Enrico Avancini, Christian Andres, Thomas Feurer, Stephan Buecheler and Ayodhya N. Tiwari

### **Abstract**

For highest efficiency Cu(In,Ga)Se<sub>2</sub> thin film solar cells the V-shaped bandgap grading can result in residual transmission through the absorber layer and parasitic absorbance in the Mo back contact. In order to improve the back contact reflectance, absorbers were grown in a multi stage process on Mo/Al/InZnO substrates. Additionally, ultrathin layers of Mo and Mo-Se<sub>x</sub> were introduced at the InZnO-absorber interface. Effects of the different back contacts on device performance, absorber morphology and composition are characterized and discussed. Finally, a numerical model is proposed to understand the experimentally observed increase in device current density of 0.3-0.8 mAcm<sup>-2</sup>.

### **1. Introduction**

Recent progress in highly efficient Cu(In,Ga)Se<sub>2</sub> (CIGS) based thin film solar cells has been driven by the introduction of absorber post deposition treatments with the alkali elements Na, K, Rb and Cs leading to increased device voltages and efficiencies as high as 22.6%<sup>[1, 2]</sup>. Most attempts to increase the current-densities of high efficiency devices on the other hand have involved a replacement of the CdS buffer (and ZnO window layer) by higher bandgap materials<sup>[3, 4]</sup> or a replacement of the conventional ZnO based transparent conductive oxides (TCO) with a higher mobility material both in order to reduce parasitic absorption in the UV and near infrared (NIR) spectral range. Recently, we have shown other strategies to improve the near band edge absorption in bandgap graded absorber either by increasing the absorber Cu content<sup>[5]</sup> or by widening the region of minimum band-gap (notch)<sup>[6] [7]</sup>. Here, we present implementation of Mo/Al/metal-oxide structure at the back contact in order to increase the back contact reflectance and hence the device current density.

Alternative back contact designs aiming to improve the back contact reflectance have been investigated mostly in view of their application in devices with thin absorber layers of around or less than 1 µm thickness. To do so, Mo was replaced by alternative metals such as W, Ta or Nb<sup>[8]</sup> or dielectrics such as ZrN<sup>[9, 10]</sup>, Al<sub>2</sub>O<sub>3</sub> or MgF<sub>2</sub><sup>[11]</sup> layers were introduced at the CIGS/Mo interface and in all cases improved rear contact reflectance was reported to some degree. In addition, texturing of the rear contact to enhance light trapping was proposed<sup>[12, 13]</sup>. Thicker absorbers >2 µm were thereby usually only discussed as a limiting case or references.

However, in solar cells with highest efficiencies a double grading of the energy band gap is targeted in the CIGS absorber layer. As a consequence of the V-shaped grading, the effective thickness of absorber material with band gap close to the minimum is well below 1 micron. Such thin band gap notch regions allow residual transmission in the NIR range and in combination with the highly absorbing Mo back contact to a considerable current loss.

Therefore, we focus on the implementation of a back contact reflector in highly efficient absorbers of conventional thickness  $>2\text{ }\mu\text{m}$  with energy bandgap double grading. We report the introduction of a novel Al/ InZnO (IZO) back contact on SLG/Mo substrates. From preliminary simulation (see **SI 1**) we estimate that the achievable current gain for a device with graded absorber is around  $1\text{ mAcm}^{-2}$  with an IZO/Al layer combination. More extensive simulations for a variety of back contacts with increased reflectance were reported recently<sup>[14]</sup>. Room temperature sputtered IZO was chosen because of the rather low NIR absorption as well as its amorphous/flat morphology. Also, we study how thin Mo or MoSe<sub>x</sub> interlayers at the IZO/CIGS interface affect the device properties. Such interlayers were reported to be mandatory for growth on metal oxides in order to improve the interface resistance<sup>[15-18]</sup>. Finally, Al was chosen because of the suitable optical properties and its expected benign<sup>[19]</sup> effect in case that residual diffusion into the absorber layer would occur.

## 2. Experimental:

**Figure 1** displays the different back contact designs considered here. First, a layer of 500 nm Mo was sputtered onto SiO<sub>x</sub> (alkaline diffusion barrier) coated soda lime glass (SLG) substrates. Then  $\sim 100\text{ nm}$  Al was thermally evaporated by electron beam deposition. The layer thickness was controlled by quartz crystal monitor. For samples A, B and C a layer of IZO (In<sub>0.893</sub>Zn<sub>0.107</sub>O<sub>x</sub>) with 260 nm thickness was deposited by room temperature (RT) pulsed DC magnetron sputtering. The resistivity of the IZO in the as deposited state was found to be in the range  $\rho = 5 \times 10^{-4}\text{ }\Omega\text{cm}$ . Thicknesses of IZO was chosen based on preliminary optical modeling by transfer matrix method (TMM) aiming to maximize the expected current density, see supplementary material S1. In all cases the same oxide thickness was chosen to facilitate comparison of the samples. Then, for samples B and C a layer of 2.6 nm Mo was deposited by RF sputtering at RT. Finally, sample C was annealed for 10 min at 450 °C in a rapid thermal processing (RTP) system in N<sub>2</sub> atmosphere with addition of  $\sim 200\text{ mg}$  of elemental Se at a base pressure of 625 mBar. In preliminary test on SLG it was observed that such RTP treatment can transform the metallic Mo to NIR transmissive material, presumably a MoSe<sub>x</sub> compound. Notably, Mo was observed to remain metallic when exposed to Se in a simulated CIGS deposition environment. This is likely related to the reduced Se partial pressure as compare to the RTP process. In addition, one reference sample REF with conventional SLG/SiO<sub>x</sub>/Mo back contact was fabricated. Substrate size in all cases was 2.5 cm x 5 cm.

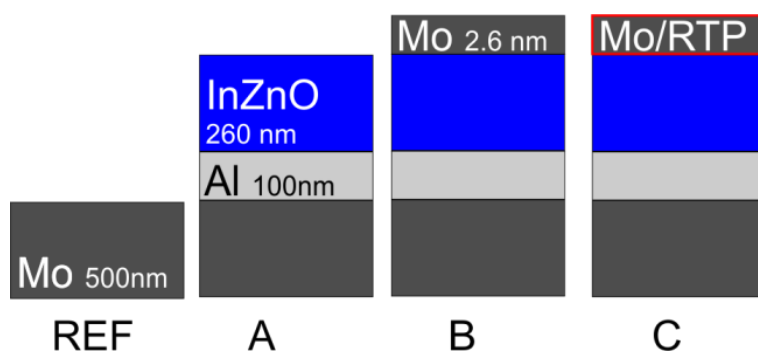


**Figure 1:** Schematic representation of thin film stacks that were implemented as back contacts in CIGS solar cells.

The CIGS absorber layers were then deposited in one single run by multi stage co-evaporation from elemental sources at substrate temperatures around 450 °C compatible with deposition on flexible polyimide. In order to isolate the expected effects of the back contact variations on the apparent series resistance, only NaF but no other alkali-fluoride was added in a post deposition treatment (PDT). Details on the absorber deposition process can be found elsewhere <sup>[6]</sup>. The absorber metal ratios were estimated for each sample individually by means of X-ray fluorescence (XRF) from the intensity of the  $K_{\alpha}$  emission lines. The devices were finalized by deposition of ~50 nm CdS from chemical bath followed by nominally 60 nm ZnO and 100 nm Al:ZnO (2 wt% of  $Al_2O_3$ ) by RF magnetron sputtering. Ni/Al grids were thermally evaporated through a metallic mask and for each substrate 6 cells of ~0.57 cm<sup>2</sup> area were defined by manual scribing. More details on device fabrication can be found in Reference<sup>[11]</sup>.

Compositional depth profiles were measured by time-of-flight secondary ion mass spectrometry (SIMS, ION-TOF GmbH TOF SIMS) with an  $O^{2+}$  sputter ion source for depth profiling and a primary  $Bi^+$  ion gun for analysis. Secondary electron microscopy and quantitative EDX (Bruker, Quantax) were measured at 10/20 keV respectively without any conductive coating. The solar cell photovoltaic parameters were characterized by means of current-voltage (JV) measurements in 4 terminal configuration under simulated AM1.5G conditions at 25 °C. External quantum efficiency measurements (EQE) with a spectral resolution of approximately 5 nm were done by using lock-in technique under halogen bias illumination of about 0.2 sun intensity. The total reflectance R on finished devices was measured on spots of ~0.23 cm<sup>2</sup> area with a UV-3600 Shimadzu UV-VIS-NIR spectrophotometer equipped with an integrating sphere. Grid shading ratios were around 4.5 % for JV and 2 % for EQE and reflectance measurements.

### 3. Results:

#### 3.1 Influence of back contact design on opto-electrical device properties

Dark and illuminated JV curves of the best efficiency samples for each case are displayed in **Figure 2 a)** and the corresponding PV parameters are compiled in **Table 1**. The reference sample yields an efficiency of 17.3 % with a current density of 32.1 mAcm<sup>-2</sup>. Notably, for all samples these values were obtained without KF or RbF PDT and without deposition of an anti-reflective coating (ARC). Highly efficient samples with RbF-PDT and ARC will be presented in section 3.3.

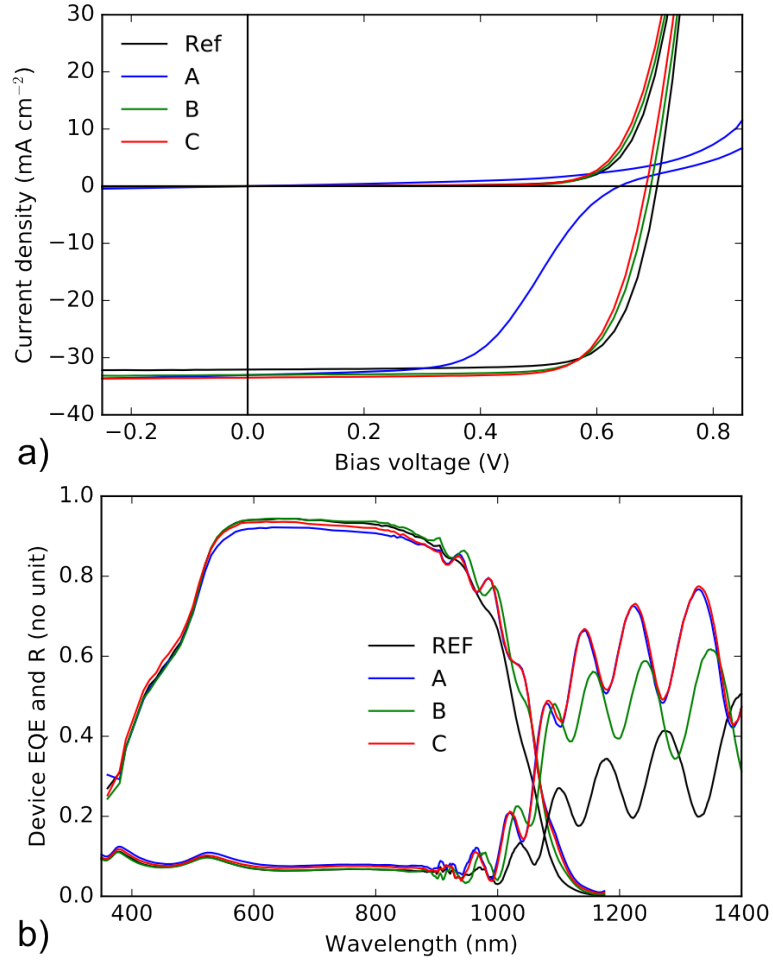
Sample A, grown without Mo interlayer, displays current blocking in forward bias direction. Similar observations in case of ITO back contacts were explained with an unfavorable band alignment between the absorber and the oxide layer<sup>[15]</sup>. In contrast, samples B and C show diode behavior, confirming that a thin layer of Mo respectively MoSe<sub>x</sub> enables formation of a more ohmic contact as was reported before <sup>[15-18]</sup>.

Table 1 shows that samples B and C yield efficiencies comparable to the REF case. Both show reduced  $V_{oc}$  and FF in comparison to the REF case. Furthermore, it can be seen that these losses are compensated by a  $J_{sc}$  increase of about 1 mAcm<sup>-2</sup>. The 1-diode model parameters

extracted from curve fits suggest that the reduced FF for B and C can be related to an apparent series resistance  $R_s$  that is increased by about  $0.5 \Omega\text{cm}^2$ . The saturation current  $J_0$  and ideality factor  $A$  on the other hand appear smaller than for the reference case, indicating the benign influence on the junction recombination properties. More extended statistics for the PV parameters can be found in **SI 2**.

EQE and reflectance measurements on the same set of devices are presented in **Figure 2 b)**. The UV-VIS parts of the EQE and reflectance spectra are similar in cases REF, B and C indicating comparable CdS growth and similar properties of the window/TCO layer stack. For sample A the UV-VIS EQE is somewhat decreased mainly due to an increased reflectance in that region, which partially can be explained by a somewhat larger grid shadowing (+1.2% of total area compared to REF). Additionally, it is possible that the back contact barrier described above might reduce photo carrier extraction.

More importantly, all modified back contact structures feature increased NIR EQE and reflectance as compared to the reference. First, the EQE is increased and more pronounced interference fringing is observed in the 900 nm -1100 nm range. Second, the average device reflectance in the region above 1000 nm is increased compared to the reference case. In the range above 1200 nm the reflectance is increased by approximately 20 abs.% for sample B and by approximately 30 abs.% for samples A and C as compared to the reference sample. Finally, the NIR EQE onset for A, B and C is found to be shifted towards longer wavelengths. In order to quantify this shift, estimates for the apparent absorber bandgaps were derived from a Tauc fit  $(eV * \ln(1 - EQE))^2$  of the EQE curves in the value range [0.3, 0.9], see Table 1. A difference of around 20 meV was found which is similar, or in case B even more than the observed reduction in  $V_{OC}$  indicating that the  $V_{OC}$  loss did not increase for cases B and C. In the following these findings are discussed in view of more detailed optical and compositional characterization.



**Figure 2:** **a)** Dark and AM 1.5 illuminated JV curves of the best devices for all four sample configurations. **b)** EQE and R spectra as measured on the same devices. The NIR signals are increased for cases with back reflectors.

**Table 1:** PV parameters of the JV curves in Figure 1a) representing the best cells obtained for each sample. The  $R_s$ ,  $R_p$ ,  $J_0$  and  $A$  were obtained from 1-diode model fitting. Full parameter statistics is given in **SI 2**.

Sample	$V_{oc}$ [mV]	$J_{sc}$ [mAcm <sup>-2</sup> ]	FF [%]	$\eta$ [%]	$R_s$ [ $\Omega$ cm <sup>2</sup> ]	$R_p$ [k $\Omega$ cm <sup>2</sup> ]	$J_0 \cdot 10^{-6}$ [mAcm <sup>-2</sup> ]	$A$	$E_{G,Tauc}$ [eV]
REF	703	32.1	76.5	17.3	0.3	1.6	1.9	1.65	1.19
A	640	33.1	67.2	13.5	-	-	-	-	1.17
B	693	33	75.5	17.3	0.6	1.6	0.9	1.55	1.17
C	685	33.5	75.1	17.2	0.7	1.3	0.7	1.51	1.17

### 3.2 Influence of back contact design on absorber layer growth

In order to estimate the integral absorber metal ratios  $[Ga]/([Ga]+[In])$  (GGI) and  $[Cu]/([Ga]+[In])$  (CGI) XRF measurements were done on finished devices. If the In signal would be taken into account, the GGI and CGI would be underestimated due to the In containing back contacts. To avoid this, the GGI and CGI were calculated from XRF Cu/Se and Ga/Se ratios (see **SI 3** for detailed description of analysis). It was found that all samples, independent of the back contact have very similar GGI and CGI around 0.41 and 0.87, respectively

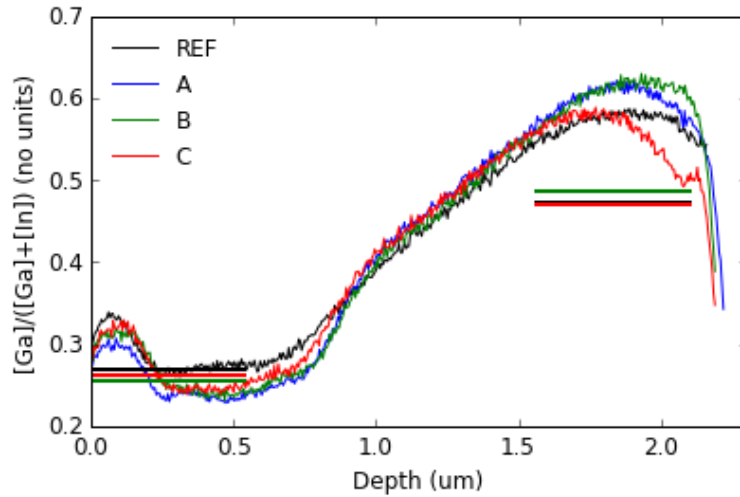


**Figure 3:** GGI depth profiles derived from SIMS measurements and scaled with the respective integral GGI as obtained from XRF. It can be seen that for cases A, B and C the Ga contents in the notch are reduced and somewhat increased towards the rear part of the absorber. The horizontal lines indicate GGIs as derived from EDX at 20 keV measured from front and rear side of the absorber layers. A similar trend as for SIMS can be observed.

In Figure 2b) a redshift of the EQE onset for the cases A, B and C was observed when compared to the REF case. Thus, in order to estimate the minimum bandgaps, GGI depth profiles were calculated from SIMS measurements. The leading and trailing edges of the absorber layer were defined to be at the sputter times where the SIMS count rate for Ga reaches half plateau values. Within that range, the Ga/In SIMS yield ratio  $\gamma$  was scaled until the integral SIMS  $GGI_{int,SIMS} = \sum Ga / (\sum Ga + \gamma \sum In)$  reached the aforementioned GGI obtained from XRF. For absolute scaling, the layer thickness was extracted from SEM measurements. Notably, very similar gradings are obtained if layer boundaries are derived from Cu or Se half maximum positions in analogous manner. The GGI profiles in **Figure 3** show that in all cases double graded absorbers with a GGI minimum (notch) were obtained, typical for the multi-stage deposition process <sup>[20]</sup>. The curves suggest that for the cases with modified back contacts, the minimum GGI level is reduced when compared to the REF case which is in qualitative agreement with the shifted EQE onset shown above. As a complementary measurement, estimates for the front and rear GGI were established by EDX with 20 keV acceleration voltage. The frontside measurements were performed on CIGS pieces etched by diluted HCL to remove the ZnO and CdS layers (10%, 1' sonication). The backside spectra were measured on the delaminated slabs of absorber. Based on CASINO <sup>[21]</sup> simulations, the EDX information depth (here 1/2 of maximum photon yield position) at 20 keV can be estimated to be around 500

nm from the sample surface. Hence, the horizontal lines in Figure 3 show the EDX derived GGI values for the different samples (same colors as SIMS profiles). Their position along the x-axis gives an indication for excitation range of the EDX signal. It can be seen that the EDX estimates qualitatively reproduce the differences in front and rear GGIs between the REF and the other samples.

A possible explanation for the observed difference in GGI grading can be that a modified sample IR emissivity and also the increased NIR reflectance of samples A, B and C reduce the heating from the source side as compared to the more absorptive Mo back contact for the REF case. Notably, in order to reach the nominal measured sample temperature the substrate heating had to be increased slightly if substrates with reflectors were co-processed. A somewhat reduced surface temperature in case of the samples with reflector could lead to reduced Ga interdiffusion and thus more pronounced Ga grading.

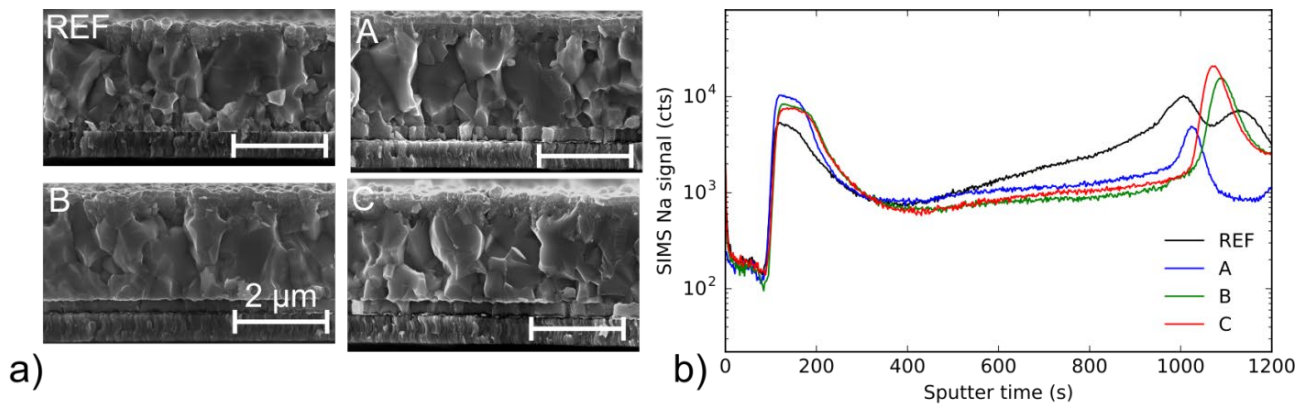


**Figure 4:** **a)** Cross section SEM micrographs of all samples. Absorber layer thickness in all cases was similar and in the range 2.1-2.2 μm. The Al and IZO layers are visible at the rear contact. **b)** The Na content as measured by SIMS is increased in the rear half for the REF sample as compared to the others.

Next, we discuss the influence of the different back contacts on absorber morphology. **Figure 4 a)** shows SEM micrographs of the device cross sections for all samples. Looking at the absorber layers first, it can be seen that all cases show typical grain sizes in the micrometer range. For the absorbers grown on the alternative back contact structures it appears that more grains of larger size are found in the rear part of the layer than for the REF case. A close up of the top interface region on the other hand shows, that for samples with reflector a layer with reduced crystal size of about ~100 nm thickness can be observed at the absorber surface.

The corresponding SIMS Na profiles are presented in **Figure 4 b)** (the absorber layers extend from about 100 s to 1000 s sputtering time). The pronounced Na peaks around 1000 s are located at the IZO/absorber interface. It can be seen that the Na content in the rear half of the absorber layers A, B and C is reduced significantly when compared to the REF sample. The Na distribution as observed in the REF case is similar to the typical one observed in layers grown on Mo substrates. As the Na was supplied during a PDT and the substrate SLG was coated

with a  $\text{SiO}_x$  diffusion barrier no significant difference in Na supply from the substrate during the growth is expected. It was observed that Na mostly aggregates at grain boundaries<sup>[22, 23]</sup>, thus the observation of smaller crystallites and increased Na content in the rear of samples A, B and C are inline. In turn, during the PDT less Na could be incorporated as the density of grain boundaries is reduced. On the other hand, the Na distributions at the IZO/absorber interface also show differences. Quantitative comparison of the Na concentrations at these different interfaces is not reliable, thus we cannot exclude another scenario in which the IZO back contact could act as Na sink reducing the absorber Na content after the PDT.

The Na content is found to be increased in the front part of the absorbers A, B and C. As mentioned above this goes along with a reduced crystal size. Furthermore, it can be observed that in this top layer the SIMS Cu signal is reduced by about 10-20% (see **SI 4**). We note that, for simultaneous growth on sets of 2.5 cm x 5 cm substrates with and without reflectors, a fluctuation of the measured sample temperature is observed that is in phase with the substrate rotation. This fluctuation can be due to the sample positioning on the substrate holder but possibly also stem from the aforementioned differences in substrate temperature. These effects hinder a well-controlled process, especially detection of the second stoichiometry point in case of co-processing of REF and modified substrates. We note, that the differences in absorber grading were observed also in a very similar type of experiment as the one described here, i.e. this effect is reproducible. The differences in the absorber surface morphology and composition on the other hand were less pronounced. This indicates that the differences observed at the absorber surface might be highly dependent on the details of a specific process, especially during the third stage. For these reasons, we cannot give a conclusive model of the effects of the substrate and back contact layer stack on absorber growth at the moment.

The back reflector layers Al/IZO are visible in Figure 4 for the samples B, C and D and their thicknesses can be estimated to be <100 nm for Al and approximately 260 nm for IZO. Figure 4a) also indicates that the IZO layer changes from amorphous in the as deposited state to a polycrystalline structure. Also variations of grain sizes are observed not only between the different samples, but in case of sample B also from one side of the substrate to the other. By SIMS measurements no Al impurities were detected in the bulk of the absorber but the Al counts in the IZO layer and at the IZO/absorber interface tended to be increased where the IZO showed larger grains. In the specific case of sample B a correlation between a decreased device performances (especially FF) with increased degree of IZO granularity and Al content in the IZO is observed (see large, systematic spread of FF for sample B in **SI 2**). These results indicate that the processing does affect the microstructure of the IZO layers which is plausible as the crystallization temperature of IZO is reported to be in the around 500 °C, i.e. close the substrate temperature during CIGS processing<sup>[24]</sup>.

### 3.3 Application in high efficiency devices

Highly efficient devices are expected to be most susceptible to slight deterioration of the electronic properties. Therefore exploring the approach on highly efficient devices gives a sensitive test for its compatibility with high quality device electronics. In order to explore if the novel back contact is compatible with our high efficiency baseline process, we present results from another batch of samples where the absorber thickness was 3  $\mu\text{m}$  and underwent RbF PDT. Furthermore  $\text{MgF}_2$  ARC was deposited on both samples. **Table 2** presents PV parameters of a reference and a sample with back contact of type B deposited in the same run. Similarly to the present series, with reflector we observe increased  $J_{\text{SC}}$  while again the  $V_{\text{OC}}$ ,  $J_0$  and A were somewhat decreased with reflector. The reference shows rather low parallel resistance and thus also a bit reduced FF. Overall, an efficiency as high as 19.9% could be realized with a device grown on an IZO based back reflector, showing that the concept can be successfully implemented in highly efficient devices.

**Table 2:** The table shows PV parameters of a reference and a device with back contact of type B. The values represent best cells obtained on these samples. Full statistics of the parameters is given in **SI 2**. In this case RbF-PDT and MgF ARC was applied to both samples.

Reflector	$V_{\text{OC}}$ [mV]	$J_{\text{SC}}$ [ $\text{mAcm}^{-2}$ ]	FF [%]	$\eta$ [%]	$R_s$ [ $\Omega\text{cm}^2$ ]	$R_p$ [ $\text{k}\Omega\text{cm}^2$ ]	$J_0 \cdot 10^{-6}$ [ $\text{mAcm}^{-2}$ ]	A
REF	726	35.8	74.8	19.5	0.18	1.7	20	2.0
Type B	721	36.5	75.6	19.9	0.55	2.4	1.6	1.7

#### 4. Discussion

In the following, we analyze the origin of the gain in current density observed for samples A, B and C. In order to do so, the devices were modeled in the framework of the transfer matrix method (TMM<sup>[25]</sup>) under the assumptions of flat layers, fully coherent light propagation and ideal collection. Shortcomings of these assumptions will be discussed below.

**Figure 5** displays simulated EQE and reflectance curves for all back contact structures introduced above. In **SI 1** the detailed descriptions of the model stacks are presented. The (n,k) datasets for the different layers were taken from<sup>[26-29]</sup>, see details in **SI 1**. Furthermore, **SI 5** shows simulated and measured EQE and reflectance curves for each sample individually. For the simulations, the layer thicknesses of Al:ZnO, ZnO, CIGS and IZO were estimated from SEM measurements. Thickness of CdS was estimated by fitting the UV range of the EQE spectra and confirmed with SEM. For the Mo interlayer in case of sample B, the nominal thickness of 2.6 nm was used in the simulation. This thickness was estimated from fitting the layer thickness to reflectance and transmittance data measured on a Mo layer deposited on a glass substrate with identical sputter parameters and using (n,k) values presented elsewhere<sup>[26]</sup>. For sample C, we assume full transformation of Mo to  $\text{MoSe}_2$  with a thickness increase by a factor 4 (based on observations in preliminary experiments). For the Al layer we take the nominal

thickness of 100 nm as determined by profilometer measurements of Al layers on glass substrate.

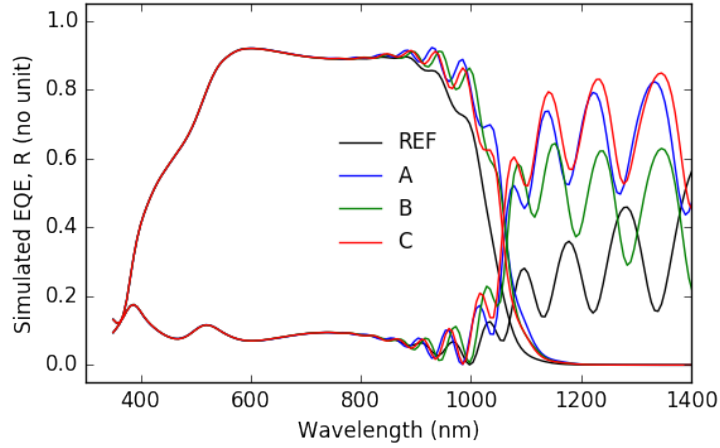


**Figure 5:** Simulated EQE and reflectance curves for cases REF and A, B, C. Details of the optical model are given in the text and in **SI 1**.

Comparing the simulations to the measurements in Figure 2 b), it can be seen that the main characteristics of the four samples are qualitatively reproduced. Improved NIR reflectance and more pronounced EQE fringes in the range 900-1100 nm are apparent for cases with added back reflector.

In the REF case the simulations give accurate reproduction of the NIR range of reflectance and EQE curves, see Figure **SI 5.1 a)**. Some deviation can be observed in the onset of the EQE indicating that the minimal bandgap energy as estimated from SIMS and XRF might be somewhat overestimated in case of the REF sample. Thus, we expect that the following analysis gives a lower bound for the current gain achieved from implementation of the back reflector.

Some differences between simulations and the measurements can be observed. First, the simulation overestimates the UV-VIS reflectance but underestimates the EQE by about 5 % in that range as compared to the measurements. This is mainly due to the assumption of flat surfaces in contrast to optically smoothened transitions in case of real layers with surface/interface roughness. Introduction of a Bruggeman effective medium<sup>[30]</sup> layer was found to improve accuracy in the UV-VIS range but does not considerably affect the relevant NIR region. Thus, to reduce the complexity of the model no EMA roughness layers are included in the following discussion.

Second, the most notable differences observed are the somewhat more pronounced amplitudes of the EQE fringes and especially the up to 10% higher average EQE level in the 900-1100 nm range in the simulations see Figures **SI 5.1 a)-d)**. Essentially, this difference can

originate from a reduced charge carrier collection for samples A, B and C and from a non-sufficient accuracy of the optical model. Further discussion of these scenarios is given in the **SI 5**.

Finally, we give quantitative estimate for the lower boundary for the current gains due to introduction of the back contact reflector. For that purpose, we calculate the current density difference due to changing the bandgap grading by means of TMM, see **Table 3**. For all cases, the back contact model of sample B was fixed. It can be noted that for the other back contacts very similar differences between the different gradings were obtained. It can be seen that the change in grading alone may only account for an increase of current density in the range 0.2-0.7  $\text{mAcm}^{-2}$ . In comparison to the measured current gains of around 1  $\text{mAcm}^{-2}$  this gives an effective current increase of about 0.3-0.8  $\text{mAcm}^{-2}$  due to the back contact reflectors alone.

**Table 3:** The table shows a summary of simulated  $J_{sc}$  for the different band gap gradings of samples A, B and C while the back contact model was fixed to the one of sample B. In each case, the second column shows the calculated current and the third column the relative increase due to the different bandgap gradings alone as compared to the reference.

GGI grading used for simulation*	$J_{sc}$ ( $\text{mAcm}^{-2}$ )	$\Delta J_{sc}$ compared to REF ( $\text{mAcm}^{-2}$ )
REF	33.28	-
A	33.92	+0.64
B	33.84	+0.56
C	33.49	+0.21

\* In all cases the back contact model of type B was used.

## 5. Conclusion and outlook

The data presented demonstrate that the current density of solar cells with 2-3  $\mu\text{m}$  thick and graded  $\text{Cu(In,Ga)Se}_2$  absorbers can be increased by the introduction of a Al/IZO/Mo or Al/IZO/MoSe<sub>x</sub> back contact reflector stack. A lower bound for the realized current gain due to introduction of the back contact reflector was estimated to be between 0.3-0.8  $\text{mAcm}^{-2}$  when compared to a reference sample grown on Mo. These findings suggest that an increase in the back contact reflectance – even for thick absorbers – can help to improve the device efficiency. The introduction of the Al/IZO layers at the back contact can lead to a more pronounced GGI grading with reduced minimum Ga concentrations if deposition rates during CIGS growth are not adapted. The observed slight decrease of  $V_{oc}$  can be explained by the decreased minimum band gap, i.e. the  $V_{oc}$  deficit remains unchanged. The reported FF loss on the other hand appears to originate from an increase in the apparent series resistance and seems correlated to the IZO deposition conditions. Overall, similar efficiencies were obtained on reference samples and samples with Al/IZO back reflector.

Based on TMM modeling of the devices the optical improvement from implementation of back reflectors was studied. We find that the internal reflection at the back may not be as efficient as expected from simulations. On the other hand, analysis of the internal quantum efficiency of the device - under consideration of all parasitic losses - suggests that carrier collection losses could be limiting the EQE in samples with optical reflector. Further experiments with re-optimized grading are necessary to study these effects in more detail. Also, further optimization of the back contact IZO and thin Mo interlayer could further reduce residual absorption and increase the back contact homogeneity and conductance.

The approach provides a step towards light trapping strategies in highly efficient absorbers. It provides a highly reflective back contact and preserves decent electronic back contact properties. Thus, in combination with appropriate substrate texturing we expect that a further current gain could be realized based on the present findings.

### **Acknowledgements**

Funding has been received from the Swiss Federal Office of Energy (SFOE contact SI/501145-01), Swiss National Science Foundation (SNSF contract 200021\_149453/1), Swiss State Secretariat for Education, Research and Innovation (SBFI contract REF-1131-52107), the Competence Center for Energy and Mobility (CCEM) in the ETH-Domain (CONNECT-PV project) and the European Union's Horizon 2020 research and innovation program under grant agreement No 641004 (Sharcs25).

## Supplementary information:

### SI 1: TMM model of device stacks

For the TMM simulations, the devices were modeled as stacks of flat layers. For the absorber, the different GGI grading presented in Figure 3 were discretized in slices of 50 nm thickness. For the other layers, thicknesses were derived from SEM measurements. The table below compiles model stacks used to model the devices with the different back contacts as shown in Figure 1. Additionally, for all materials references for the optical constants (n,k) are given. Figure S1 shows influence of the oxide thickness on the expected current gain for different cases.

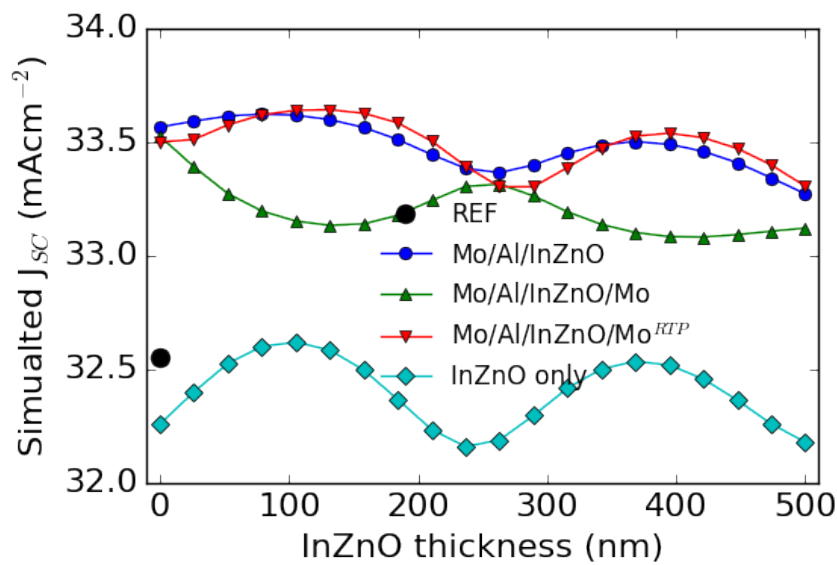


**Figure SI 1:** Simulated  $J_{sc}$  in dependence on IZO thickness for the configurations B and C and additionally for the case where only the oxide was added. For these simulations, the grading of the reference sample was used, see Figure 3. The maxima and minima in the minima originate from interference conditions for waves reflected at front and backside interface of the oxide spacer layer. For an estimated refractive index of 1.85 (at 1000 nm where increased reflectance is most relevant) this would suggest a reflectance maximum at  $\lambda_{max} = \frac{1000 \text{ nm}}{4n} = 135 \text{ nm}$  which is in good agreement with the simulation. Additionally, it can be seen that the phase of the  $J_{sc}$  oscillation is shifted by one half phase in case of sample B. This is likely due to the low-high refractive index phase shift at the first Cu(In,Ga)Se<sub>2</sub>/(thin)Mo interface in contrast to all other cases where the refractive indices are decreasing upon leaving the absorber layer.

It is apparent that control of the oxide thickness is critical to achieve maximum current gain. Also, it can be seen that the maximally achievable current gain is somewhat bigger than 1 mA cm<sup>-2</sup> in case of a MoSe<sub>2</sub> back contact interface.

**Table SI 1:** The table compiles the model stacks for samples REF, A, B and C that were modeled by TMM. Thicknesses and references for (n,k) values for each layer are given.

Sample	REF	A	B	C
ZnO:Al		95 nm <sup>[26]</sup>		
ZnO		61 nm <sup>[26]</sup>		
CdS		47 nm <sup>[26]</sup>		
CIGS		~2.2 $\mu\text{m}$ , see Fig 3 <sup>[26]</sup>		
MoSe <sub>2</sub>	6 nm <sup>[27]</sup>	-	-	10.4 nm <sup>[27]</sup>
Mo	-	-	2.6 nm <sup>[28]</sup>	-
InZnO	-		260 nm*	
Al	-		100 nm <sup>[29]</sup>	
Mo		500 nm <sup>[28]</sup>		

\*(n,k) derived from fitting of R%, T% measurements of 500 nm thick films deposited on glass.

## SI 2: PV parameter statistics

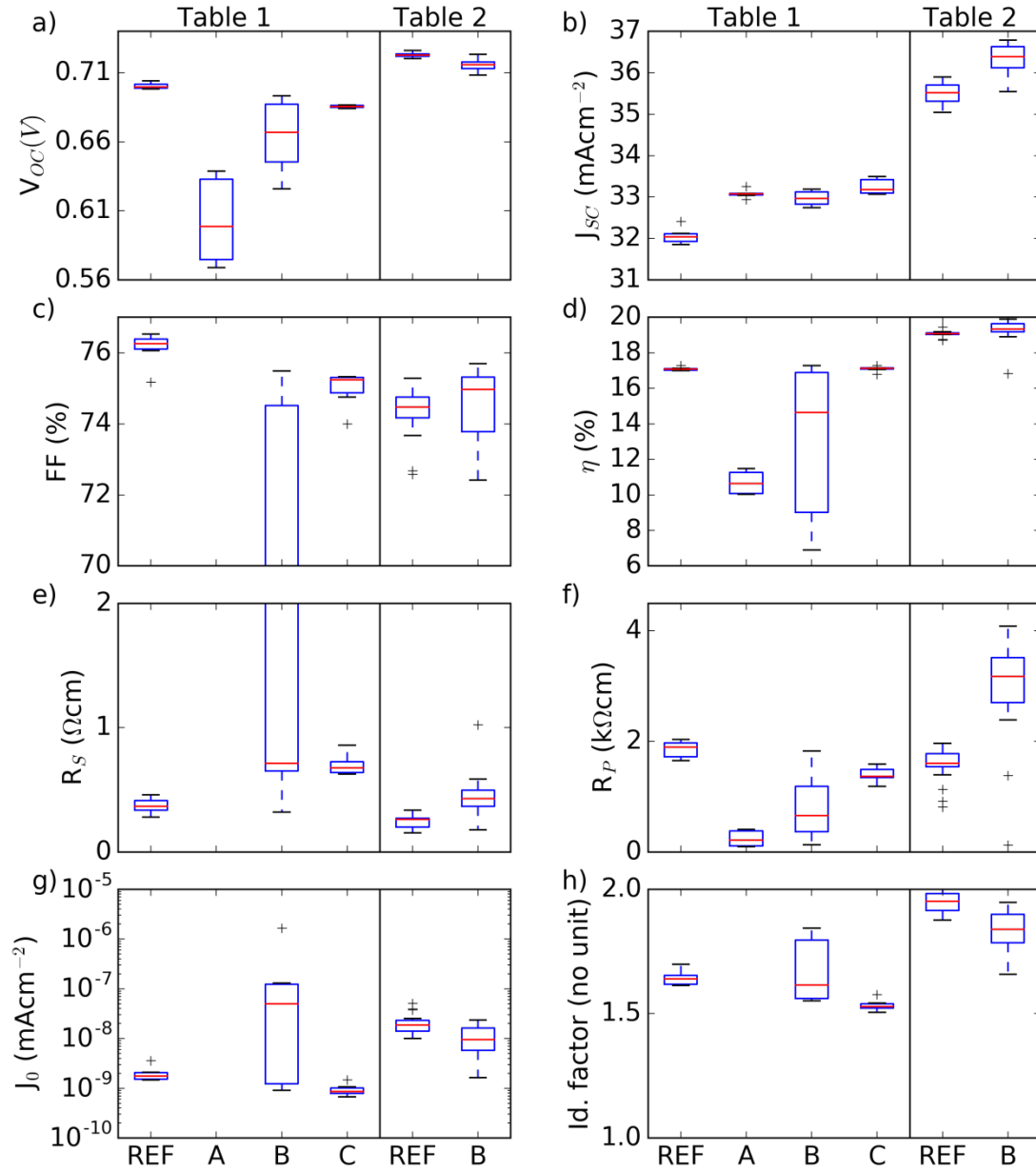


**Figure SI 2:** The figure displays distributions of PV parameters for the samples introduced in Tables 1 (left hand side of vertical line) and Table 2 (right hand side of vertical line). It can be seen that all samples with back reflectors show an increase in current density in the range  $+1 \text{ mAcm}^{-2}$ . The large spread in FF observed for samples of type B is not randomly distributed but consistently decreases from one side of the substrate to the other. We presume this to be related to deposition details of the IZO layer and a more detailed investigation of this inhomogeneity is topic on ongoing investigation, see also main text. No  $J_0$  and A are shown for sample A due to strongly non-diodic behavior. Additionally it can be noted, that samples with back contact of type C were reproduces in another separate deposition run showing similar

improvement in NIR EQE as reported here and again efficiencies similar to the reference devices. Same holds for samples of back contact type B that were reproduced in two additional deposition runs.

### SI 3: GGI estimation from XRF without use of In signal

First, the XRF yield factors for the Cu, Ga and Se peaks were determined from a number of films including CGS layers. Then, valid estimates for the Cu/Se and Ga/Se ratios can be calculated. Finally, knowing these ratios and under the assumption that the absorber can be represented as mixture of  $\text{Cu}_2\text{Se}$  and  $(\text{In,Ga})_2\text{Se}_3$  it is possible to calculate the CGI and GGI values.

To do so the layer is represented as a mixture of  $\{\text{Cu}_2\text{Se}\}_k + \{\text{In}_2\text{Se}_3\}_l + \{\text{Ga}_2\text{Se}_3\}_m$ . Then if the ratios

$$u = \frac{\text{Cu}}{\text{Se}} \text{ and } v = \frac{\text{Ga}}{\text{Se}}$$

are known from XRF, the GGI and CGI can be written as

$$\text{GGI} = \frac{3v}{2-u} \text{ and } \text{CGI} = \frac{3u}{2-u}.$$

Notably, this procedure reproduces CGI and GGI values as obtained from conventional XRF data interpretation as well as ICPMS measurements on a number of samples in the compositional range  $0.15 < \text{GGI} < 0.6$  and  $0.8 < \text{CGI} < 1$ .

### SI 4: SIMS Cu profiles

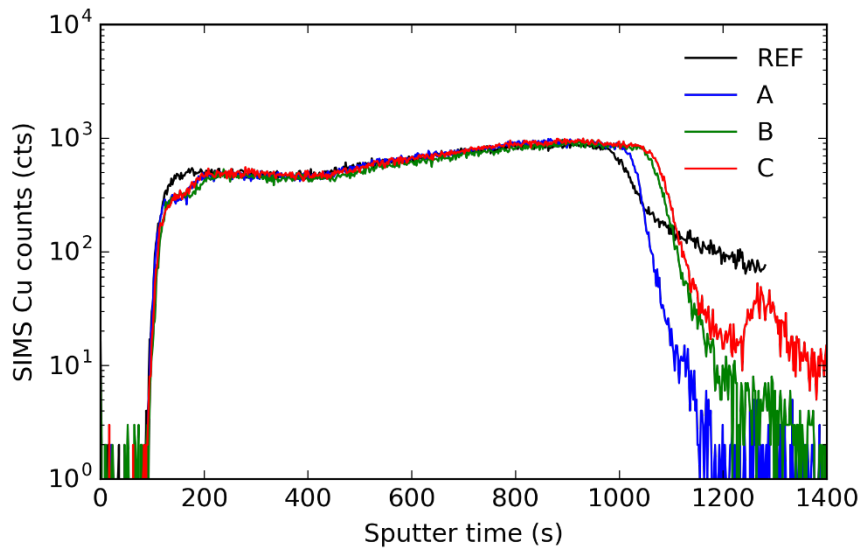


**Figure SI 4:** SIMS Cu profiles as measured on the four samples introduced in section 3.1. For samples with modified back contact the Cu content at the front surface (around 100 s sputtering time) appears reduced by around 20%.

## SI 5: Discussion of modeled and simulated EQE and R for all samples

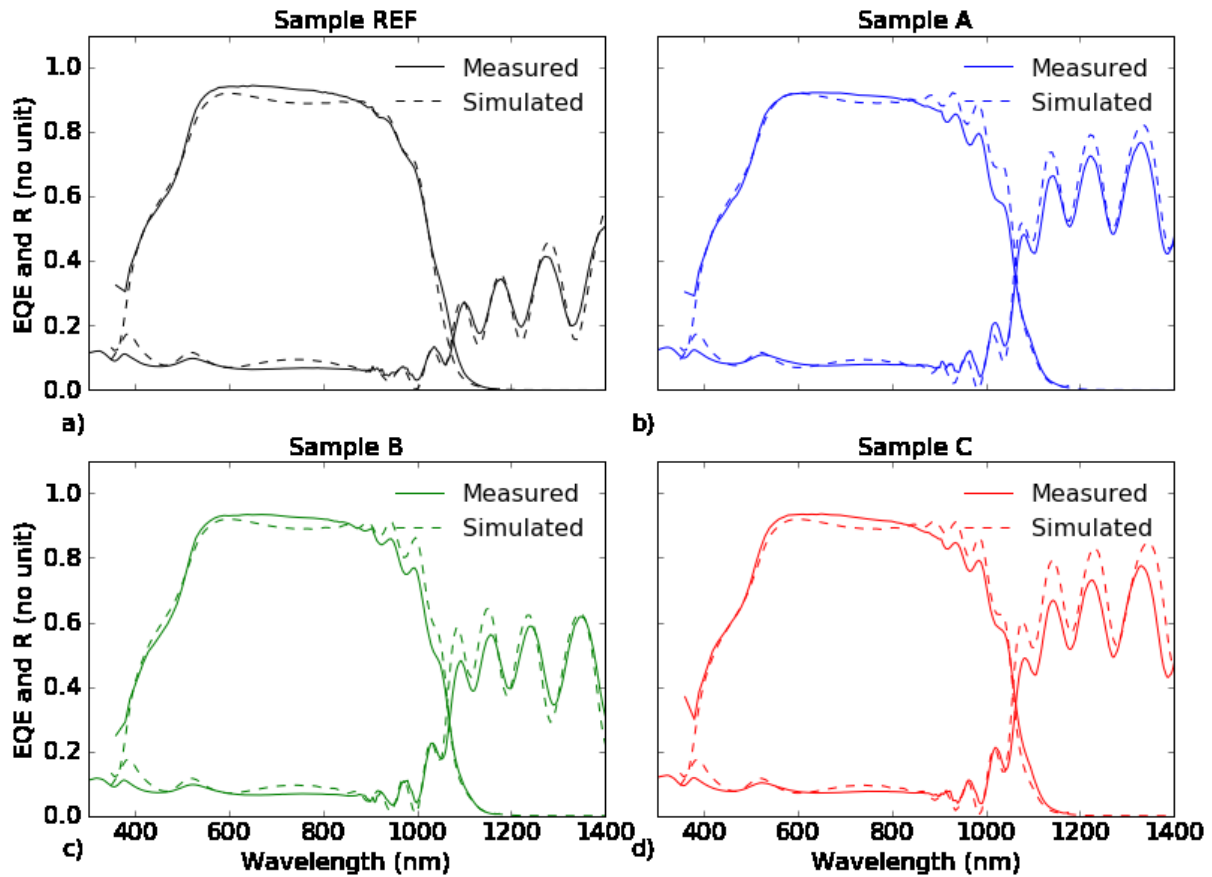


**Figure SI 5.1:** Simulated (solid lines) and measured (dashed) EQE and R curves for all samples.

As mentioned in the main text, for samples with modified back contact the simulated EQE is higher in the 900-1100 nm range than the measured ones, see **Figure SI 5.1**. This can essentially originate from deficiencies in the optical model and from reduced carrier collection efficiency in cases with reflectors. Here we discuss aspects of these two hypotheses.

First, the optical model does not include surface roughness and consequently no effects of light scattering are considered. In order to assess this, Figure SI 5.2 shows the reflectance haze measured for samples REF, B and C on bare absorber surfaces.

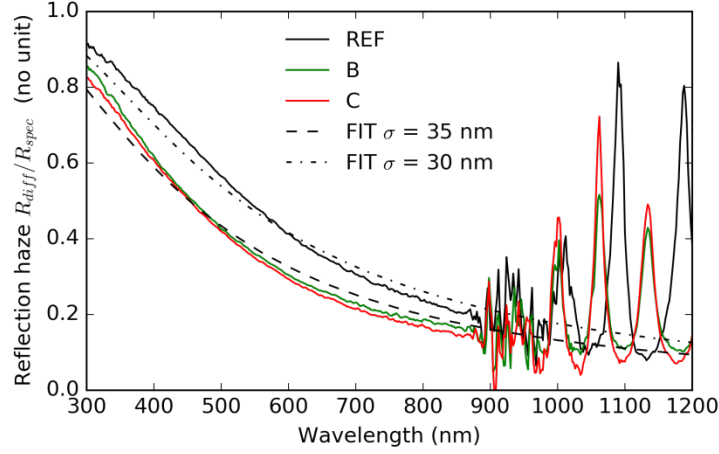


**Figure SI 5.2:** The solid lines show measured ratio of diffuse over specular reflectance (haze) for samples REF, B and C. The dashed lines show model fits according to <sup>[31]</sup> with two different surface roughness parameters  $\sigma$ .

The haze for the reference sample is found to be higher, indicating a larger optical roughness  $\sigma$ . The difference in roughness can be quantified by fitting the data with expressions from Krc et al. <sup>[31]</sup>, see dashed lines in SI 3.2. We find values for  $\sigma$  of around 30 nm and 35 nm for the reference and samples B and C, respectively. For the fitting, the refractive index of CIGS was assumed to be 2.84 and the correction factor  $c_t$  was set to one, see <sup>[31]</sup> for details. This can be relevant, as a larger surface roughness implies increased diffuse transmission into the absorber which would result in longer effective optical paths of the scattered light and therefore a potentially increased EQE.

In order to give quantitative estimate of this effect, equation 5 in reference <sup>[31]</sup> was used to calculate the diffuse and specular surface transmissions from air ( $n=1$ ) into the absorber ( $n=2.84$ ) ( $T_{diff}, T_{spec}$ ) with the roughness values from Figure SI 3.2. It is assumed that the front interface leads to lambertian scattering. Further, we consider a wavelength  $\lambda$  where the absorbance (for specular propagation) of the absorber layer is  $A_{spec}(\lambda) = x$ . Then, the light intensity that is scattered into an angle  $\theta$  can be integrated to obtain the average diffuse absorbance

$$A_{diff}(\lambda) = 2 \int_0^{\pi/2} \sin(\theta) \cos(\theta) \left(1 - \exp\left(-\frac{\log(1-x)}{\cos(\theta)}\right)\right) d\theta. \quad (\text{Eq. SI 5.1})$$

This spherical integral (hence  $\sin(\theta)$ ) averages the angle dependent absorbance  $A(\theta) = 1 - T(\theta) = 1 - \exp\left(-\frac{\log(1-x)}{\cos(\theta)}\right)$  with weights  $\cos(\theta)$  due to lambertian scattering and 2 is a normalization factor from integration of the lambertian term only. Consequently, an estimate of the EQE for a given surface roughness  $\sigma$  can be written as

$$EQE(\lambda; \sigma) = T_{spec}(\sigma) * A_{spec}(\lambda) + T_{diff}(\sigma) * A_{diff}(\lambda). \quad (\text{Eq. SI 5.2})$$

For  $A_{spec} = 0.9$  (around 1000 nm) this analysis predicts a difference in EQE of less than 2% absolute due to difference in surface roughness which would be less than the observed differences of about 10% between measurements and simulations for the different samples. However, this analysis can only provide a rough estimate and without detailed knowledge of the scattering mechanism we currently cannot give a more rigorous treatment.

Another possible discrepancy can be that the optical properties of the individual back contact layers (IZO, Al, MoSe<sub>x</sub>) might change during absorber deposition leading to an overestimation of the internal reflectance for the alternative back contacts. Based on the good reproduction of the reflectance in the 900 nm - 1100 nm range this however seems less likely.

Yet another possible mechanism explaining the discrepancy between simulated and experimental EQE for samples A, B and C in the 900-1000 nm range is a reduced charge carrier collection as compared to the REF case. This could be due to the lower minimum Ga content/bandgap in cases A, B and C or due to a different extend of the space charge region related to the observed differences in the absorber surface morphology. Both explanations can potentially reduce the charge extraction from the notch region. Thus, we attempt to estimate the internal quantum efficiency (IQE) i.e. the ratio between extracted charge carriers and those generated in the absorber only.

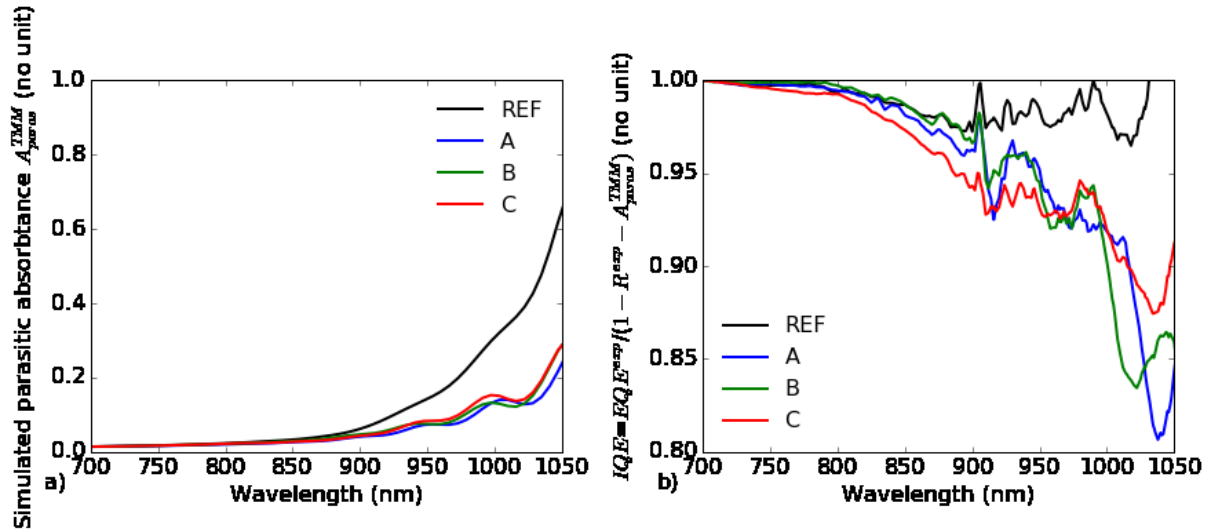


**Figure SI 5.3: a)** Simulated integral parasitic absorbance  $A_{paras}^{TMM}$  in the NIR range in all layers except for the absorber itself. **b)** Estimates of the internal quantum efficiency calculated according to Equation SI 3.3.

In case of semi-opaque layers with consideration of parasitic absorption in front and back electrodes it was recently proposed that a combination of experimental ( $EQE^{exp}$ ,  $R^{exp}$ ) and TMM based data (parasitic absorption in front and back layers  $A_{paras}^{TMM}$ ) can give an approximation of the IQE<sup>[32]</sup>. We used the expression

$$IQE = \frac{EQE^{exp}}{(1 - R^{exp} - A_{paras}^{TMM})} \quad (\text{Eq. SI 5.3})$$

where  $A_{paras}^{TMM}$  was calculated by means of TMM for the same device models introduced above. The curves of  $A_{paras}^{TMM}$  are presented in Figure SI 3.3 a). For the REF case, the Mo layer was found to be the largest source of parasitic absorption in the 900 – 1100 nm. For cases with back reflector the IZO and Al layers still dominate absorption in that range but to a lower extend. Furthermore, in all cases the front contact AZO contributes to parasitic absorption. Curves for the IQEs according to Equation SI 3.3 are presented in Figure SI 3.3 b). The data are only shown up to 1050 nm. Above 1050 nm the absorber layer becomes more transparent and the denominator of Eq. SI 3.3 (see below) is strongly determined by the simulated  $A_{paras}^{TMM}$  and thus minor simulation inaccuracies can lead to large errors.

The comparison shows that for the REF case the IQE is close to unity up to 1000 nm, while in case of samples A, B and C it appears to be reduced by more than 5%. We note that this analysis i.e. the values for  $A_{paras}^{TMM}$  are again susceptible to errors in the optical modeling. In order to check the robustness of the calculation, we artificially increased the back contact absorbance by 20% for the samples with reflectors which is more than the observed difference between simulated and measured reflectance in the range above 1200 nm. Still, we find that samples with reflector showed systematically reduced IQE around 1000 nm. EQE measurements were also performed under application of 1.2 V reverse bias, but no clear difference between REF and cases B and C could be observed. This does not imply equivalent collection properties though, as the increase in the space charge region width upon biasing is dependent on the doping and defect concentrations in the region near to the pn-junction.

It can be concluded that the roughly 10% absolute discrepancy between simulated and measured EQE at 1000 nm can be due to different roughness and or collection properties which are not considered in the optical model. The analysis proposed here suggests that at least 2% can be explained by differences in roughness and a somewhat larger share by different collection properties. We note however, that the optical analysis presented only takes into account a model case for the scattering mechanism and certainly further studies are necessary to reach to a more unambiguous understanding.

## References:

1. Chirila, A., et al., *Potassium-induced surface modification of Cu(In,Ga)Se-2 thin films for high-efficiency solar cells*. Nature Materials, 2013. **12**(12): p. 1107-1111.
2. Jackson, P., et al., *Effects of heavy alkali elements in Cu(In,Ga)Se-2 solar cells with efficiencies up to 22.6%*. Physica Status Solidi-Rapid Research Letters, 2016. **10**(8): p. 583-586.
3. Friedlmeier, T.M., et al., *Improved Photocurrent in Cu(In, Ga)Se-2 Solar Cells: From 20.8% to 21.7% Efficiency with CdS Buffer and 21.0% Cd-Free*. Ieee Journal of Photovoltaics, 2015. **5**(5): p. 1487-1491.
4. Kamada, R., et al. *New world record Cu(In, Ga)(Se, S)<sub>2</sub> thin film solar cell efficiency beyond 22%*. in *2016 IEEE 43rd Photovoltaic Specialists Conference (PVSC)*. 2016.
5. Avancini, E.C., R.; Bissig, B.; Reinhard, P.; Menozzi, R.; Sozzi, G.; Di Napoli, S.; Feurer, T.; Nishiwaki, S.; Buecheler, S.; Tiwari, A. N., *Impact of compositional grading and overall Cu deficiency on the near-infrared response in Cu(In,Ga)Se<sub>2</sub> solar cells*. Progress in Photovoltaics, 2016. **25**(3): p. 233-241.
6. Nishiwaki, S.F., T.; Bissig, B.; Avancini, E.; Carron, R.; Buecheler, S.; Tiwari, N.T., *Precise Se-flux control and its effect on Cu(In,Ga)Se<sub>2</sub> absorber layer deposited at low substrate temperature by multi stage co-evaporation*. Thin Solid Films, 2016. **in press**: p. 18-22.
7. Sozzi, G., et al., *Analysis of Ga grading in CIGS absorbers with different Cu content*. 2016 Ieee 43rd Photovoltaic Specialists Conference (Pvsc), 2016: p. 2279-2282.
8. Orgassa, K., H.W. Schock, and J.H. Werner, *Alternative back contact materials for thin film Cu(In,Ga)Se-2 solar cells*. Thin Solid Films, 2003. **431**: p. 387-391.
9. Malmstrom, J., S. Schleussner, and L. Stolt, *Enhanced back reflectance and quantum efficiency in Cu(In,Ga)Se-2 thin film solar cells with a ZnO back reflector*. Applied Physics Letters, 2004. **85**(13): p. 2634-2636.
10. Schleussner, S., et al., *Reactively sputtered ZnO for application as reflecting back contact in Cu(In,Ga)Se-2 solar cells*. Thin Solid Films, 2009. **517**(18): p. 5548-5552.
11. Vermang, B., et al., *Employing Si solar cell technology to increase efficiency of ultra-thin Cu(In, Ga)Se-2 solar cells*. Progress in Photovoltaics, 2014. **22**(10): p. 1023-1029.
12. Yin, G.C., et al., *Optoelectronic Enhancement of Ultrathin CuIn<sub>1-x</sub>Ga<sub>x</sub>Se<sub>2</sub> Solar Cells by Nanophotonic Contacts*. Advanced Optical Materials, 2017. **5**(5).
13. Yin, G.C., et al., *Well-Controlled Dielectric Nanomeshes by Colloidal Nanosphere Lithography for Optoelectronic Enhancement of Ultrathin Cu(In,Ga)Se-2 Solar Cells*. Acs Applied Materials & Interfaces, 2016. **8**(46): p. 31646-31652.
14. Poncelet, O., et al., *Optimisation of rear reflectance in ultra-thin CIGS solar cells towards >20% efficiency*. Solar Energy, 2017. **146**: p. 443-452.
15. Nakada, T., et al., *Novel device structure for Cu(In,Ga)Se-2 thin film solar cells using transparent conducting oxide back and front contacts*. Solar Energy, 2004. **77**(6): p. 739-747.
16. Rostan, P.J., et al., *Formation of transparent and ohmic ZnO : Al/MoSe<sub>2</sub> contacts for bifacial Cu(In,Ga)Se-2 solar cells and tandem structures*. Thin Solid Films, 2005. **480**: p. 67-70.
17. Mattheis, J., et al., *Carrier collection in Cu(In,Ga)Se-2 solar cells with graded band gaps and transparent ZnO : Al back contacts*. Solar Energy Materials and Solar Cells, 2007. **91**(8): p. 689-695.
18. Simchi, H., et al., *Improved Performance of Ultrathin Cu(InGa)Se-2 Solar Cells With a Backwall Superstrate Configuration*. Ieee Journal of Photovoltaics, 2014. **4**(6): p. 1630-1635.
19. Marsillac, S., et al., *High-efficiency solar cells based on Cu(InAl)Se-2 thin films*. Applied Physics Letters, 2002. **81**(7): p. 1350-1352.
20. Chirila, A., et al., *Highly efficient Cu(In,Ga)Se-2 solar cells grown on flexible polymer films*. Nature Materials, 2011. **10**(11): p. 857-861.
21. Drouin, D., et al., *CASINO V2.42 - A fast and easy-to-use modeling tool for scanning electron microscopy and microanalysis users*. Scanning, 2007. **29**(3): p. 92-101.
22. Cadel, E., et al., *Atom probe study of sodium distribution in polycrystalline Cu(In,Ga)Se-2 thin film*. Acta Materialia, 2010. **58**(7): p. 2634-2637.

23. Cojocaru-Miredin, O., et al., *Atomic-scale distribution of impurities in CuInSe<sub>2</sub>-based thin-film solar cells*. Ultramicroscopy, 2011. **111**(6): p. 552-556.
24. Yaglioglu, B., H.Y. Yeom, and D.C. Paine, *Crystallization of amorphous In<sub>2</sub>O<sub>3</sub>-10 wt % ZnO thin films annealed in air*. Applied Physics Letters, 2005. **86**(26): p. 261908.
25. Byrnes, S.J., 1603.02720. arXiv.org, 2016.
26. Carron, R., et. al., *Inhouse Measurements; Manuscript in preparation: Refractive indices of layers and optical simulations of Cu(In,Ga)Se<sub>2</sub> solar cells*. in preparation, 2017.
27. Evans, B.L. and Hazelwoo.Ra, *Optical and Structural Properties of Mose<sub>2</sub>*. Physica Status Solidi a-Applied Research, 1971. **4**(1): p. 181.
28. Hara, T., et al., *Quantitative Assessment of Optical Gain and Loss in Submicron-Textured CuIn<sub>1-x</sub>Ga<sub>x</sub>Se<sub>2</sub> Solar Cells Fabricated by Three-Stage Coevaporation*. Physical Review Applied, 2014. **2**(3): p. 034012.
29. Palik, E.D., *Handbook of Optical-Constants*. Journal of the Optical Society of America a-Optics Image Science and Vision. Vol. 1. 1984. 1297-1297.
30. Bruggeman, D.A.G., *Calculation of different physical constants of heterogen substances I Dielectric constants and conductivity of mixtures from isotrop substances*. Annalen Der Physik, 1935. **24**(8): p. 665-679.
31. Krc, J., et al., *Analysis of light scattering in a-Si : H-based solar cells with rough interfaces*. Solar Energy Materials and Solar Cells, 2002. **74**(1-4): p. 401-406.
32. Armin, A., et al., *Quantum Efficiency of Organic Solar Cells: Electro-Optical Cavity Considerations*. Acs Photonics, 2014. **1**(3): p. 173-181.